Supplemental Information

Supplementary Figure 1: Phenotype of CW mice

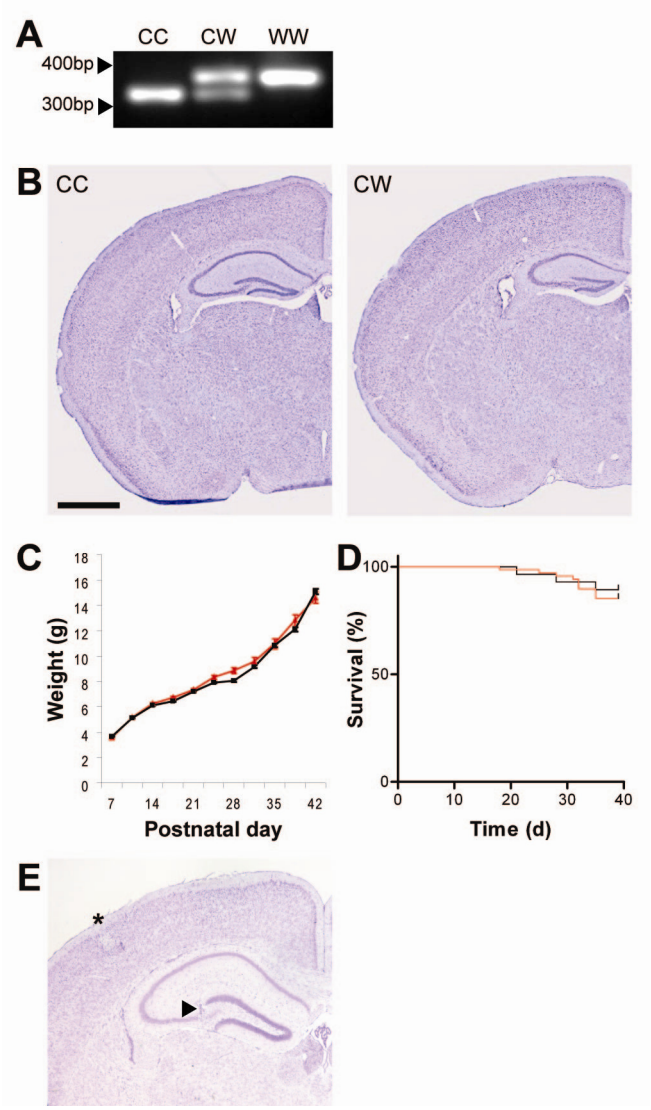

(A) Genotyping results for CC and CW mice (CC 330 bp, CW 330/360 bp and WW 360 bp)
(B) Nissl-stained CC (left) and CW brain sections (right) illustrating normal brain morphology in P16 mice.
(C) Weight gain CC (black) and CW mice (red)
(D) Survival curves CC (black) versus CW mice (red; Logrank test, P=0.62)

Supplementary Figure 2: Different expression patterns of β1(C121)-EGFP and β1(W121)-EGFP along the proximo-distal axis of the AIS

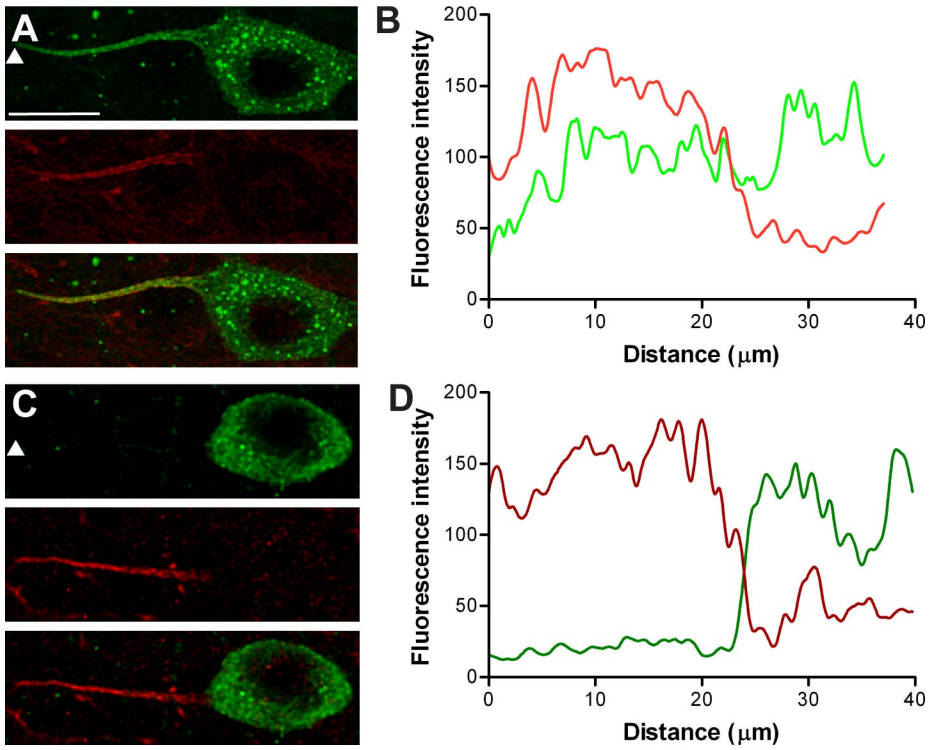

Green/ top: Virally expressed β1(C121)-EGFP (A) or β1(W121)-EGFP (C). Red/ middle: staining against Ank. Bottom: Merge of the two channels.
(A) β1(C121)-EGFP is evenly distributed along the AIS and co-localizes with Ank (arrowhead: starting point of AIS fluorescence intensity plot (B)).
(B) β1(W121) is not localized to the AIS (arrowhead: starting point of AIS fluorescence intensity plot (D)).
(C) Fluorescence intensity plot along the AIS and continuing into the soma of the neuron shown in A. β1(C121)-EGFP is high in both AIS and soma (green) while Ank is exclusively localized to the AIS (red).
(D) Fluorescence intensity plot along the AIS and continuing into the soma of the neuron shown in C. β1(W121)-EGFP is exclusively localized in the soma (green).
Scale bar 10μm

Supplementary Figure 3: β1(C121)-EGFP co-localizes with Na^+-channel α-subunits and Ank in the AIS membrane

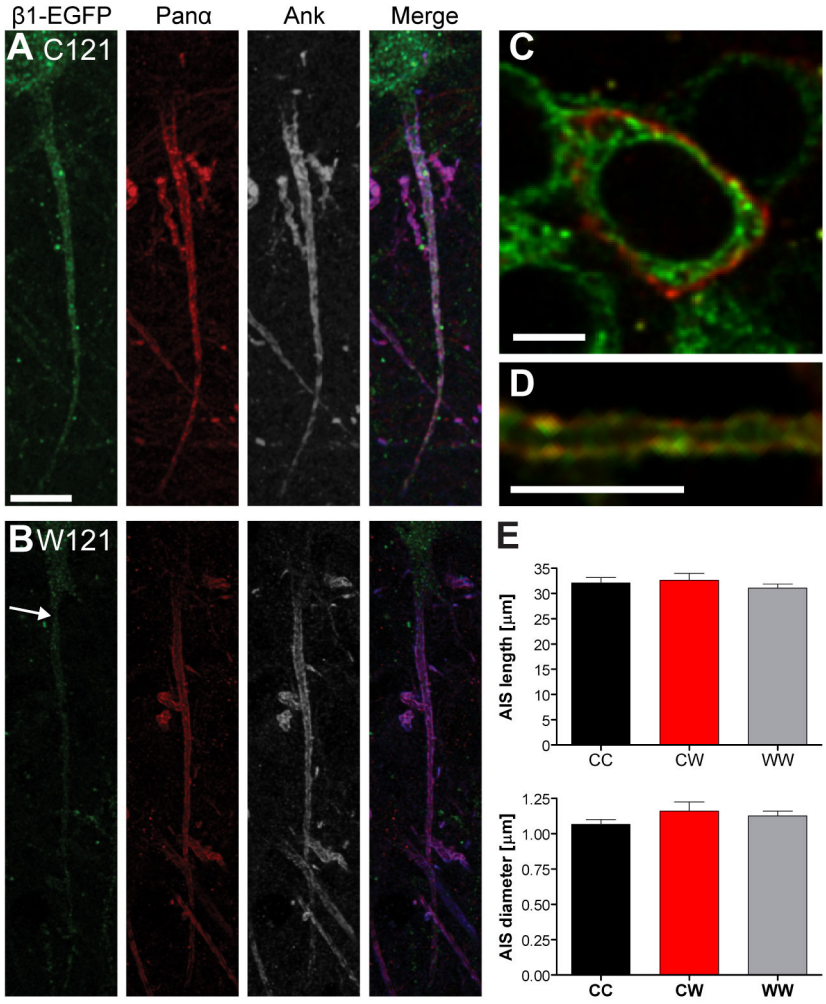

Green: Virally expressed β1(C121)-EGFP (A,C) or β1(W121)-EGFP (B). Red: staining against all Na^+-channel α-subunits (Panα). Grey: AIS visualized by staining against Ank. 'Merge' of the three channels with Ank depicted in blue.
(A) β1(C121)-EGFP is evenly distributed along the AIS and co-localizes with Na^+-channel α-subunits and Ank.
(B) β1(W121) cannot be detected in most of the AIS, except for occasional small β1(W121) clusters in proximal AIS (arrow).
(C) β1(C121)-EGFP is not detectable in the somatic plasma membrane labeled by expression of membrane-bound tdTomato (with myristoylation tag; mtdTomato, red), however, β1 may still be expressed at the somatic plasma membrane albeit in concentrations lower than at the AIS.
(D) mtdTomato was rarely observed in the AIS, presumably due to the selective filter properties of the AIS[46]. In the few cases we found mtdTomato in large caliber AISs, β1(C121)-EGFP and mtdTomato co-localized in the AIS membrane.
(E) Morphological parameters of AIS are similar in CC, CW and WW tissue (example shown: CA3). CC n=26, CW n=15, WW n=25; length P=0.67, Kruskal-Wallis-test; diameter P=0.34, Kruskal-Wallis-test).
Scale bar 5µm

Supplementary Figure 4: CW neurons are hyperexcitable

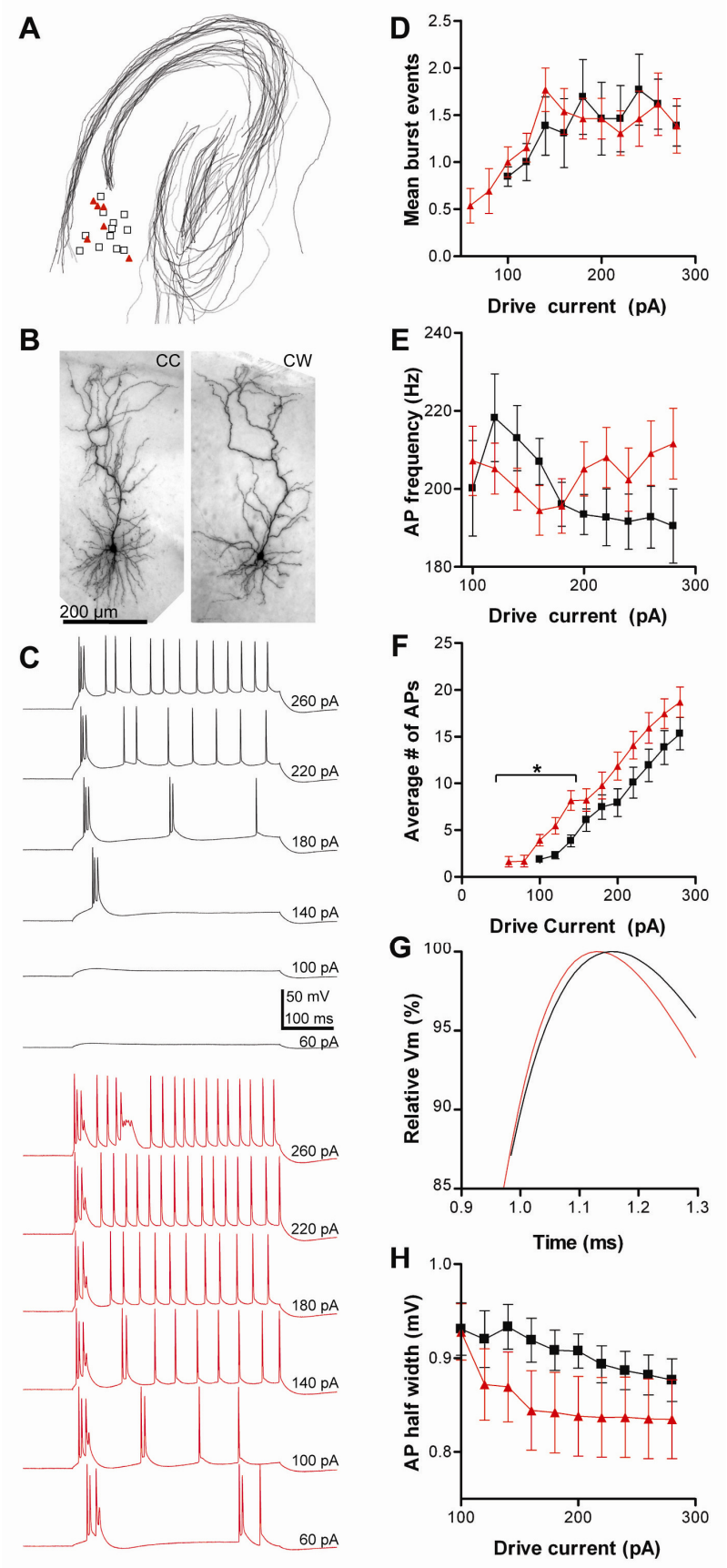

Black line/bars: CC, n=13 neurons from 8 mice; red line/bars: CW, n=13 neurons from 6 mice.

(A) Overlapping distribution of recorded neurons in subiculum, aligned relative to CA1 and DG.
(B) Examples of biocytin-filled subicular neurons.
(C) Additional examples of current clamp recordings of CC (black) and CW (red) subicular neurons. Note AP firing at lower drive current, longer bursts, higher firing frequency and higher AP amplitude in CW cell trace.
(D) Mean number of burst events (P=0.74; t-test).
(E) No difference in AP frequency during bursts (P=0.33; t-test).
(F) Combined I/O curve for burst and tonic firing (asterisks: P=0.0041 or less for multiple t-tests).
(G) AP waveforms normalized to maximum amplitude, illustrating earlier AP peak in CW neurons.
(H) AP half-width is significantly shorter in CW neurons (P=0.0002, t-test).

Supplementary Figure 5: Slowed AP kinetics at low temperature

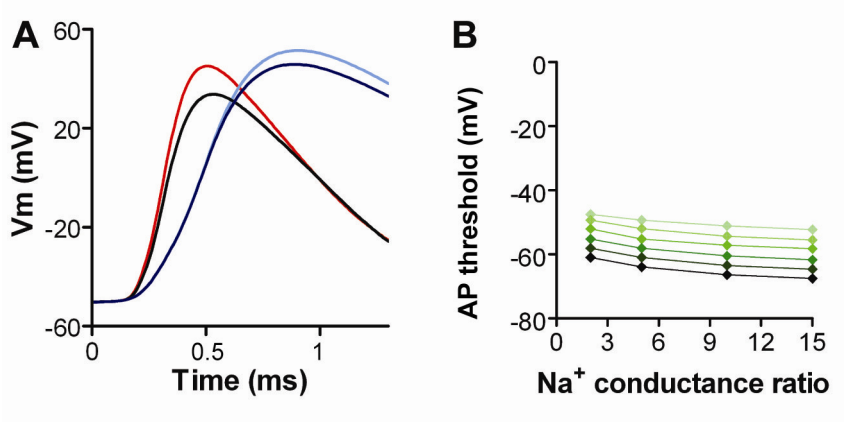

(A) Slower AP kinetics at 22 ºC (CW 34 ºC: red, 22 ºC light blue; CC 34 ºC black, 22 ºC dark blue).
(B) Model reproduces AP threshold change at the AIS (cf. Fig. 5f).

Supplemental Methods

The somatic i_{NaT} was modeled according to ref. {Migliore, 1999 #287}.

$$i_{NaT} = \bar{g}_{Na} \cdot m^3 \cdot h \cdot s \cdot (E - E_{Na})$$

with m, h. and s corresponding to the gating parameter for fast activation, fast inactivation, and slow-inactivation, respectively.

The equations describing activation were as follows:

$$\alpha_m = \frac{0.4\ ms^{-1} \cdot (E + 30\ mV - \Delta V_{1/2})}{1 - \exp(-(E + 30\ mV - \Delta V_{1/2})/7.2\ mV)}$$

$$\beta_m = \frac{0.124\ ms^{-1} \cdot (E + 30\ mV - \Delta V_{1/2})}{1 - \exp((E + 30\ mV - \Delta V_{1/2})/7.2\ mV)}$$

$$\tau_m = \frac{1}{Q(T) \cdot (\alpha_m + \beta_m)},$$

if $\tau_m < 0.02\ ms$ then $\tau_m = 0.02\ ms$

$$m_\infty = \frac{\alpha_m}{\alpha_m + \beta_m}$$

The parameter $\Delta V_{1/2}$ was used to introduce a shift in the midpoint of the activation curve. This parameter was zero for the somatic i_{NaT}.

The equations describing fast inactivation were as follows:

$$\alpha_h = \frac{0.03\ ms^{-1} \cdot (E + 45)}{1 - \exp(-(E + 45)/1.5\ mV)}$$

$$\beta_h = \frac{-0.01\ ms^{-1} \cdot (E + 45\ mV)}{1 - \exp((E + 45\ mV)/1.5\ mV)}$$

$$\tau_h = \frac{1}{Q(T) \cdot (\alpha_h + \beta_h)}, \text{ if } \tau_h < 0.5\ ms \text{ then } \tau_h = 0.5\ ms$$

$$h_\infty = \frac{1}{1 + \exp((E + 50\ mV)/4\ mV)}$$

The equations describing slow inactivation were as follows:

$$\alpha_s = 1\ ms^{-1} \cdot \exp\left(\frac{139.24\ mV^{-1} \cdot (E + 60\ mV)}{T[K]}\right)$$

$$\beta_s = 1\ ms^{-1} \cdot \exp\left(\frac{27.85\ mV^{-1} \cdot (E + 60\ mV)}{T[K]}\right)$$

$$s_\infty = 1$$

$$\tau_s = \frac{\beta_s}{0.0003 \cdot (1 + \alpha_s)}, \text{ if } \tau_s < 10\ ms \text{ then } \tau_s = 10\ ms$$

We assumed $T_0 = 24\ ^\circ C$, the Q_{10} values were derived from {Migliore, 1999 #287}. The equilibrium potential for Na^+ was $E_{Na} = 55\ mV$. The Na^+ current at the AIS was identical to the somatic Na^+ current, but lacked the slow inactivation process. The parameter $\Delta V_{1/2}$, which produces a shift of the activation behavior, was systematically varied as described in the results section.